PCCP

# Symmetry mismatch controlled ferroelastic domains ordering and functional properties of manganite films on cubic miscut substrates



| | |
|---|---|
| Journal: | *Physical Chemistry Chemical Physics* |
| Manuscript ID | CP-ART-05-2021-001957.R1 |
| Article Type: | Paper |
| Date Submitted by the Author: | 23-Jun-2021 |
| Complete List of Authors: | Paudel, Binod; Los Alamos National Laboratory, MPA-CINT; New Mexico State University, Physics<br>Kang, Kyeong Tae; Los Alamos National Laboratory, MPA-CINT<br>Sharma, Yogesh; Los Alamos National Laboratory, MPA-CINT<br>Nakotte, H.; New Mexico State University<br>Yarotski, Dmitry; Center of Integrated Nanotechnologies,<br>Chen, Aiping; Los Alamos National Laboratory, |
| | |

Journal Name

ARTICLE

# Symmetry mismatch controlled ferroelastic domains ordering and functional properties of manganite films on cubic miscut substrates

Received 00th Dec 2018,
Accepted 00th January 20xx

DOI: 10.1039/x0xx00000x

www.rsc.org/

Binod paudel [a,b] Kyeong Tae Kang,[a] Yogesh Sharma,[a] Heinrich Nakotte,[b] Dmitry Yarotski,[a] and Aiping Chen*[,a]

We have studied the magnetotransport properties and strain release mechanisms in ferroelastic $La_{0.9}Sr_{0.1}MnO_3$ (LSMO) epitaxial thin films on $SrTiO_3$ (STO) (001) substrates with different miscut angles. The substrate miscut angle plays a critical role in releasing shear strain and has huge impact on films' properties. The strain relaxes by monoclinic distortion for films on low miscut substrates and for higher miscut substrates, the strain relaxation causes the formation of periodic twin domains with larger periodicities. We observe that the Curie temperature ($T_C$) decreases systematically, and magnetoresistance (MR) increases with increasing the miscut angle. Such changes in magnetic and transport properties could be due to the increased density of phase boundaries (PBs) with the increase of miscut angle. This work provides a way to tailor film microstructures and subsequent functional properties of other complex oxide films on miscut substrates with symmetry mismatch.

## 1. Introduction

Complex oxides have gained tremendous research interest as they exhibit intriguing functionalities such as ferromagnetism, ferroelectricity, piezoelectricity, multiferroicity, and superconductivity due to the dynamics of strongly correlated electrons present in their *d*- and *f*-orbitals.[1,2] Such functionalities in thin films, heterostructures, and nanocomposites of complex oxides can be controlled via defect engineering, strain engineering, and interface engineering.[2,3] For $ABO_3$ perovskite oxide thin films, strain engineering have been widely used to tailor the functional properties by deliberately controlling the corner sharing oxygen octahedral units, which modifies the B-O-B bond angles and bond lengths.[4,5] Therefore, lattice mismatch has been considered as one of the most critical parameters in the epitaxial growth of complex oxides. Different substrate/buffer layers constraint to the films result in (semi)coherent growth, thereby generating desired epitaxial strain and tunable functional properties.[1,2,6–8]

Besides lattice mismatch, symmetry mismatch is another critical parameter in epitaxial film growth, which could exist if the symmetry of the film and the substrate is different. The structural modifications by symmetry mismatch greatly influence the growth and consequent properties of the overlying films. One scenario that has been discussed is the growth of oxide films with the rhombohedral or orthorhombic structure on cubic substrates.[9–12] Near the interface of rhombohedral/orthorhombic film and cubic substrate, the interfacial octahedral proximity effect plays a key role in controlling functional properties via imprinting

[a] Center for Integrated Nanotechnologies (CINT), Los Alamos National Laboratory, Los Alamos, New Mexico 87545, USA
[b] Department of Physics, New Mexico State University, Las Cruces, New Mexico 88003, USA
* Email: apchen@lanl.gov

Electronic Supplementary Information (ESI) available: [details of any supplementary information available should be included here]. See DOI: 10.1039/x0xx00000x

substrate $BO_6$ octahedra rotations into the film.[13,14] For example, orthorhombic $SrRuO_3$ films on $SrTiO_3$ (STO) show tetragonal symmetry up to a thickness of 18 *uc* due to suppression of tilt angle of $RuO_6$ at the interface and changed to orthorhombic symmetry above this thickness limit.[15] Interfacial octahedral tilting of $RuO_6$ and $TiO_6$ on highly strained SRO/STO superlattices results in antiferromagnetic (AFM) transitions from the ferromagnetic (FM) phase.[16] Such an octahedral proximity effect is only confined in a few nanometers ranges near the interface of the heterostructure. In the region beyond 10 nm away from the substrate/film interface, along with lattice mismatch strain, the shear strain also comes into play. Shear strain relaxation often modulates film microstructures and functional properties significantly.[17] Periodical micro-twining has been reported to accommodate the shear strain in ferroelastic materials.[17] Growths of rhombohedral ferroic films such as $La_{0.7}Sr_{0.3}MnO_3$ on cubic STO (001) revealed four and $BiFeO_3$ (BFO) on STO(110), STO(111) revealed two and single domain variants, respectively.[18,19] Such control of domains is attributed to the symmetry mismatches and the substrate orientation. Furthermore, formation of structural twin domains in ferromagnetic films can be controlled by breaking symmetry at the substrate surfaces which requires miscut substrates.

Substrate miscut angle and direction are another critical factor in the epitaxial growth with symmetry mismatches. Single crystal substrates with large miscut angle and small terrace width offer preferential growth sites with control on growth mode, microstructure, and property that might not be achieved from other approaches. By changing the substrate miscut angle and directions, domain variants of the rhombohedral BFO films on cubic miscut STO substrates have been successfully reduced into two and mono-domains.[20,21] Such films with controlled domains have reduced leakage current in BFO. The growth of orthorhombic films on miscut STO substrates has also reduced six orthorhombic domain variants into a single one attributing to minimum surface energy.[22] Therefore, substrate miscut angle plays a critical role in determining the domain microstructure in ferroelastic systems. Although symmetry mismatch and substrate miscut angle are critical parameters in epitaxial growth, the correlation among miscut angle, microstructure modulation, and functional properties in ferroelastic oxides, especially manganites have not been well understood.[23,24] Here, we studied how substrate miscut angle modifies film microstructure via the shear strain relaxation and how microstructure modulates the magnetotransport properties of $La_{0.9}Sr_{0.1}MnO_3$ (LSMO) epitaxial films. We observed the systematic suppression on $T_C$ and enhanced CMR with the increase in miscut angles, which is due to the increased phase boundaries (PBs) near the step edges on the substrate.

## 2. Results and Discussion

It is reported that $La_{0.9}Sr_{0.1}MnO_3$ (LSMO, hereafter) doping resides at the boundary between orthorhombic and rhombohedral phases.[25] Growth of LSMO on cubic STO stabilizes with orthorhombic at room temperature but shows rhombohedral phase for higher temperatures.[26] The static Jahn-Teller (*J-T*) distortion of $MnO_6$ octahedra deforms LSMO into orthorhombic, giving lattice parameters $a$ = 5.586 Å, $b$ = 7.715 Å, $c$ = 5.540 Å.[27] The pseudocubic lattice parameters of LSMO are given by $a$ = 3.922 Å, $b$ = 3.932 Å and $c$ = 3.868 Å,[28] with lattice misfit of -0.43% and -0.69% along *a*- and *b*-directions to STO substrate, respectively. Another strain called shear strain appears on the films due to the angle change between [100] and [010] axes, and this is what makes the film distorted orthorhombic.[29] Orthorhombic LSMO with 10% Sr doping is a paramagnetic insulator and it becomes rhombohedral ferromagnetic metal with 16% Sr doping.[30]

When orthorhombic LSMO is grown on cubic STO substrate, LSMO $[110]_o$ out of plane and $[1\text{-}10]_o$, $[001]_o$ in-plane directions correspond to [001], [010], and [100] directions of cubic STO respectively,[29] as shown in Figure 1 (a). To simplify the discussion, we will use pseudocubic notion to describe orthorhombic LSMO. The substrate miscut angles ($\beta$) and directions ($\alpha$) are major parameters to achieve different growth modes and domain orientations. Substrates with $\beta \neq 0$ and $\alpha = 0$ have unidirectional steps either along STO [100] or [010] that allow films to grow with the formation of preferable domains, as shown in Figure 1(b). The growth modes will be completely different on the substrates with $\beta \neq 0$ and $\alpha \neq 0°$. For $\alpha < 45°$, the films will have two growth modes (domains) due to the steps along STO [100] and [010] directions, as shown in Figure 1 (c).[31] For example, length of the steps along [100] direction is larger than that of along [010] implies that the more domains will form along [100]. However, the formation of isotropic domains towards *A* and *B* directions are equally probable if the two steps have the same lengths, i.e., $\alpha = 45°$. This saw tooth-like substrate structure with $\alpha = 45°$ also corresponds to miscut angle along [110] direction.

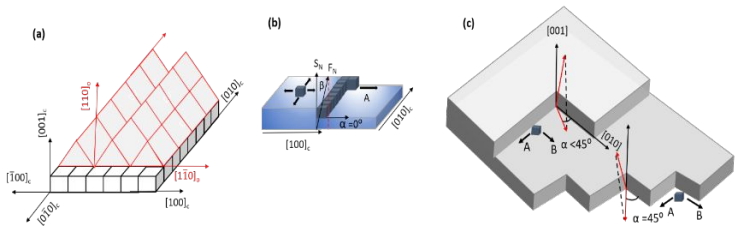


Figure 1: (a) Growth of orthorhombic LSMO on cubic substrate STO. The indices 'o' and 'c' in the crystal directions correspond to LSMO and STO. (b) Miscut substrates with zero miscut direction ($\alpha = 0°$) with different miscut angles $\beta$ and $\beta_1$. (c) Miscut substrate with non-zero miscut direction ($\alpha \neq 0°$). Steps along [100] and [010] directions show two preferred growth direction as shown as A and B.

To study the film quality and structural evolution of films, XRD $2\vartheta$-$\omega$ scans and rocking curves (RCs) are performed. Figure 2(a) shows $2\vartheta$ - $\omega$ scans of the films on 0.1°, 2°, 4° miscut substrates, which are epitaxial, *c*-axis oriented with only peaks along (00*l*) directions, without the presence of any other phases. The out-of-plane lattice parameter for all films is around 3.87Å, indicating almost negligible (-0.051%) strain for films on different miscut substrates. The film quality is also confirmed from the FWHM of the RCs ($\omega_{002}$) and are found to be 0.0672°, 0.087°, and 0.0785°, respectively. The presence of well-defined thickness Laue fringes indicates the sharp substrate-film interface. Figure 2(b) shows the film RCs around (002) reflections exhibiting the satellite peaks around the main peaks. The growth of orthorhombic LSMO films on cubic STO substrates imposes the film substrate symmetry mismatch, where the strain energy is released via the formation of periodic twin domains.[17] The existence of periodic twining is confirmed by the symmetric satellites around the main peak.[32] Nucleation of the majority of longer and anisotropic domains along [100] for larger miscut angles as confirmed from TEM.[33] Moreover, smaller splitting of $\omega$-$\omega_{00l}$ around LSMO *00l* (*l* =1, 2, 3, 4) with increasing diffraction order *l* also indicates the presence of in-plane periodic twining, Figure S1. The first order RC gives the in-plane tilt angles between two twin domains, which are calculated as 0.35°, 0.9° and 0.8° for 0.1°, 2° and 4° films, respectively indicating that film planes are more tilted for larger miscut angles, Figure S1. The spacing of the first satellite peaks ($\Delta q_x$) from the central peak also gives the minimum domain periodicity (*d*) which increases when the satellite peaks move closer to the central peaks with the increase of miscut angles.[34,35] Such minimum periodicities are determined by using the formula $d = 1/(2\Delta q_x)$.

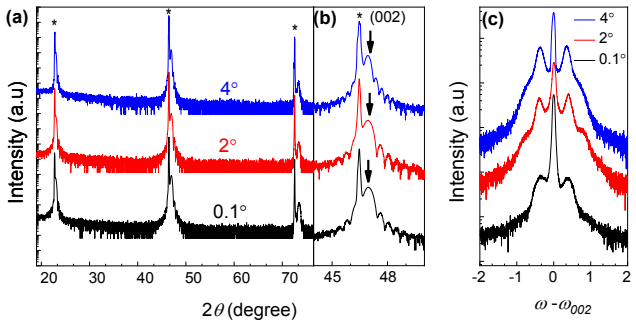


Figure 2. (a) XRD $2\vartheta$ - $\omega$ scans of films show all the peaks are out of plane oriented. Not having any other peaks indicates the films are of a single phase. (b) Scans of the films around (002) show the same film peak positions regardless of miscut angles showing miscut angles do not affect biaxial film strains. (c) RCs ($\omega$-scans) of the films around (002) peaks show the periodic twining of the films.

To observe the shear strain relaxation and visualize domain formation, reciprocal space maps (RSMs) are measured around (103) reflections by rotating samples with an increment of 90° with respect to the surface normal. All the films are coherently grown on the substrates amid the formation of ferroelastic twin domains on higher miscut films. Since the terrace widths are larger for 0.1° miscut substrate, this acts like a nominally flat substrate without formation of well-defined domains illustrated by the diffuse RSM peaks, as shown in Figure 3 (a). This film lowers the symmetry from orthorhombic to monoclinic due to difference in out-of-plane lattice parameters of (013) as compared to that of the rest of the other planes. This is also consistent with the results from RSMs around (*h*03) (*h* = 0, 1, 2, and 3), where the splitting along *l*-direction is not the same in each reflection as shown in Figure S2. Different $q_z$ values around (203) and (303) compared to (003) and (103) and unequal in-plane lattice parameters around all (*h*03) (*h* = 0, 1, 2, and 3) implies in-plane and out-of-plane tilting of twin domains in 0.1° film. For 2° film, satellites are clearly formed with domains variants decreased from four (in 0.1°) to two,[33] Figure 3(b). Majority of the domains align towards [100], which confirms the domain anisotropy in higher miscut substrates. Long-range ordered and nearly [100] oriented 1D domains in 4° films has shown by the second-order satellite peaks in Figure 3(c). Furthermore, RSMs around all (*h*03) (*h* = 0, 1, 2 and 3) in higher miscut films (2° and 4°) demonstrate that there is also in-plane tilting of the twin domains as all reflections have different $q_x$ values and similar $q_z$ around (103) reflections, which does not indicate monoclinic distortion of films. Interestingly, the increase of miscut angle has promoted the growth of only 1D twinned domains along [100] in 2° and 4° films, whereas 2D domains are prominent along [100] and [010] in low miscut (0.1°) films.[33] For 2° and 4° films, the domains along [100] are the majority, and their presence generates anisotropic domains and thereby stabilizes uniaxial magnetic anisotropy.[33]

The release of the shear strain between film and substrate results into the formation of twin domains whose ordering depends on the miscut angles.[17,33] The twin domains become more ordered and anisotropic, producing the satellite peaks owing to the decrease in terrace widths with increase of miscut angles, as shown in Figures 3 (b, c). The occurrence of broad peaks in 0.1° film shows the short range ordering of domains. However, first-order satellite peaks in 2° and the satellite peaks up to second order in 4° films have indicated that the domain correlation lengths are further increased with increasing the miscut angles from 2° to 4°.[33]

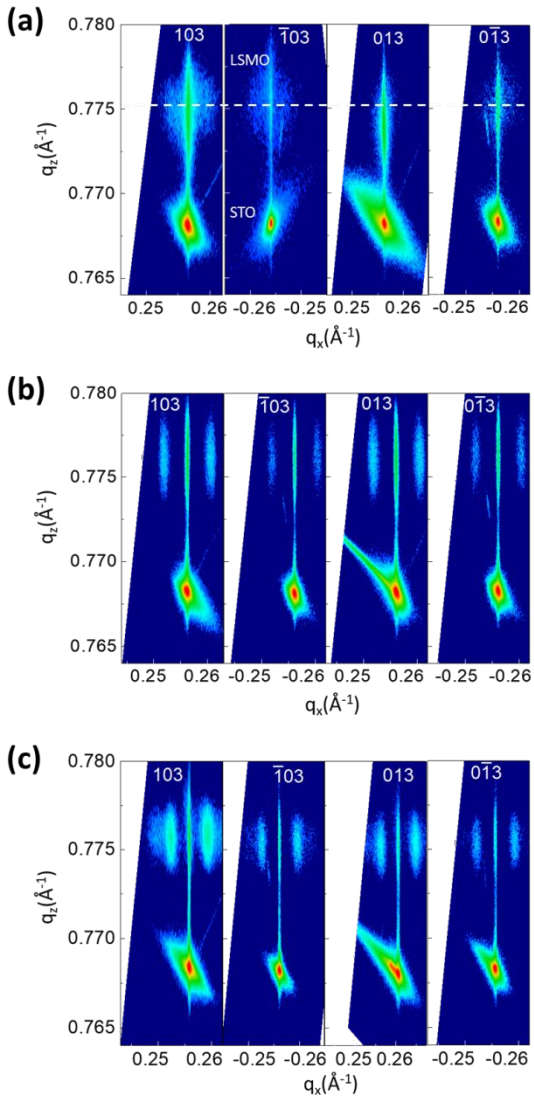


Figure 3: (a) RSMs near STO (013) of (a) 0.1° film, (b) 2° film and (c) 4° film. Film grows coherently but strain releases with (a) due to monoclinic distortion, (b) and (c) due to formation of periodic twin domains as illustrated by satellite peaks.

To study the effect of film microstructures and strains on the magnetic properties, we performed the field cooled (FC) and zero field cooled (ZFC) *M-T* measurements at 100 Oe magnetic field, applied along film in-plane direction. The $T_C$ values obtained from the measurements are 283 K, 267 K, and 253 K respectively for 0.1°, 2°, and 4° films, as shown in Figure 4. Firstly, the Curie temperatures ($T_C$) enhancement compared to the bulk LSMO (145 K) is consistent with the role of compressive strains that shortens the Mn-O bond lengths triggering Jahn-Teller distortion that lifts orbital degeneracy of $e_g$ orbitals, cation off-stoichiometry, and film microstructures.[36,37] Interestingly, $T_C$ gradually decreases with the increase of miscut angle. Since the films have similar thickness and epitaxial strain, substrate miscut angle induced film microstructure should be the main driving force for such $T_C$ modulations. Film-substrate symmetry mismatch alters the

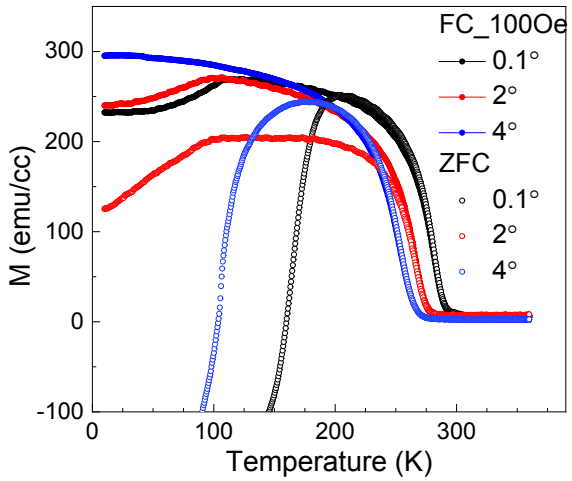


Figure 4: FC and ZFC M-T measurements for films on different miscut substrates with a magnetic field of 100 Oe. Suppression of the Curie temperature is obvious from the figure.

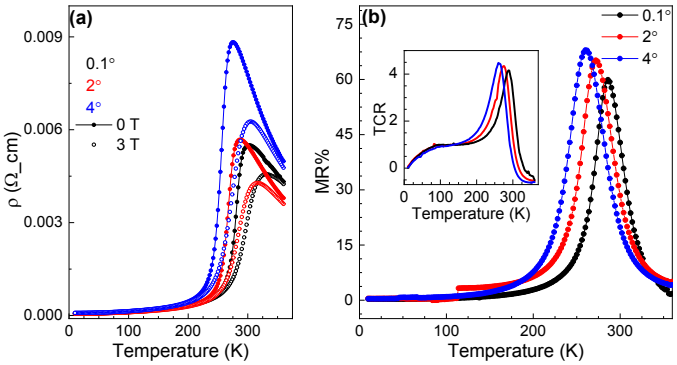


Figure 5. (a) ρ-T of the films in the magnetic field of 0 T and 3 T. (b) Temperature dependent CMR and temperature coefficient of resistances TCR for these films on different miscut substrates.

film microstructure from domain nucleation and orientation which directly modify magnetic properties. For example, the magnetization anomaly near 105K controlled by the competition between microstructure controlled magnetic anisotropy and STO antiferrodistortive phase transition.[33]

To examine the transport properties, we performed the four-probe ρ-T measurements on these samples. Figure 5a shows ρ-T curves at 0T and 3T for films on 0.1°, 2° and 4° miscut substrates. All the films show conducting behavior even though bulk LSMO is an insulator. It is often believed that the biaxial compressive strain increases the out-of-plane Mn-O bonds angles and makes them straight, which increases the $e_g$ electron hopping on manganite.[37,38] The CMR *[= (ρ(0)-ρ(H))/ρ(0)]* and *TCR [=(1/ρ(dρ/dT))]*, where *ρ(0)* and *ρ(H)* are the resistivities at zero and applied field, are shown in Figure 5b. Table 1 summarizes the $T_C$, $T_{MI}$, peak MR and TCR values

for these three samples. Consistent with the enhanced $T_C$, the enhancement in $T_{MI}$ compared to their bulk counterparts are also observed. In addition, both $T_C$ and $T_{MI}$ decrease while the peak MR and peak TCR increase with increasing substrate miscut angles.

Table 1: Summary of the magnetic and transport properties of the films on different STO miscut substrates

| Sample | 0.1° | 2° | 4° |
|---|---|---|---|
| $T_C$ (K) | 283 | 267 | 253 |
| $T_{MI}$ @0T (K) | 302 | 287 | 275 |
| $T_{MI}$ @3T (K) | 329 | 315 | 303 |
| Peak MR | 60% | 66% | 69% |
| Peak TCR | 4.2 | 4.4 | 4.5 |

Since film unit cells from two substrate terraces never have a complete registry due to symmetry breaking at the steps, formation of PBs is expected near the step terraces.[39,40] Miscut angles depend on the heights and widths of terraces as given by the formula, $tan\beta = na_{STO}/d$, where $n$ is the number of unit cells on step height, $a_{STO}$ is the lattice parameter of STO, and $d$ is the width of the substrate terraces. As the PBs are formed at the substrate step edges, the increase in the miscut angle results into smaller terrace widths thereby increasing the density of PBs. At the PB regions, the disruption of Mn-O-Mn bonds, and the modulation of such bond angles/lengths produce strong magnetic disorders that weakens the FM spin ordering.[41,42] Larger substrate miscut angle indicates the higher PB density and therefore suppressed $T_C$ and $T_{MI}$. On the other hand, MR and TCR will be enhanced because applied magnetic field aligns disordered spins at PB regions.[43]

## 3. Conclusion

In summary, orthorhombic epitaxial $La_{0.9}Sr_{0.1}MnO_3$ films are deposited on STO substrates with different miscut angles. The evolution of film microstructures depends on strain release mechanisms as the films on 0.1° miscut substrates undergoes the monoclinic distortion, whereas on 2° and 4° miscut substrates, it releases forming periodic twin domains. A systematic modification of magnetic and transport properties should be attributed to the modified Mn-O-Mn bonds length and angle near the PB, induced by substrate miscut. These results can be applied to understand the driving forces that tailor magneto transport properties of various oxide thin films on miscut substrates.

## 4. Experimental section

Pulsed laser deposition (PLD) using a KrF excimer laser (λ = 248 nm) has been utilized to synthesize $La_{0.9}Sr_{0.1}MnO_3$ films on STO substrates with miscut angles of 0.1°, 2°, and 4° and terraces are parallel to STO [100]. The samples are named 0.1° film, 2° film, and 4° film, respectively. Films were deposited at 725 °C with 100 mTorr of $O_2$ pressure. The laser fluence of 1.5 J/cm$^2$ and laser repetition rate of 1 Hz with a substrate-target distance of 6.0 cm has resulted in a growth of ~1 nm/min. After deposition, an oxygen pressure of 500 Torr was introduced into the chamber. The films were post-annealed for 30 minutes at 500°C followed by cooling down to room temperature at a rate of 5°C/min. High-resolution XRD was performed to reveal the textures, epitaxy, and strains of the samples. The thickness of these films is estimated to be 25~30 nm from Laue fringes. Reciprocal space maps (RSM) were measured to examine in-plane lattice modulations and satellite peaks resulting from tilting of the films. In order to visualize the structural modulation from domain formations, the tilt angles were measured from ω-scans for different diffraction orders. Magnetic and transport properties were measured using a physical property measurement system (PPMS, Quantum Design). The in-plane *M-H* curves were measured at 10 K, and in-plane field cooled (FC) *M-T* curves were measured in 100 Oe field from 10 K to 360 K at a scan rate of 2 K/min. The *R-T* measurements are performed with a four-probe method with four Au bars sputtered on the film surface.

## Acknowledgments

The work at Los Alamos National Laboratory was supported by the NNSA's Laboratory Directed Research and Development Program, and was performed, in part, at the Center for Integrated Nanotechnologies, an Office of Science User Facility operated for the U.S. Department of Energy Office of Science. Los Alamos National Laboratory, an affirmative action equal opportunity employer, is managed by Triad National Security, LLC for the U.S. Department of Energy's NNSA, under contract 89233218CNA000001.

## Conflicts of interest

There are no conflicts to declare.

## Authors Contributions

B.P. and A. C. conceived and designed the experiments. B. P., A. C., K. T. K. and Y.S. fabricated the samples and analyzed the properties. B. P., A.C. performed magnetotransport and XRD measurements. B.P. wrote the manuscript and all authors including B.P., K.T.K., Y.S., H. N., D.Y., and A.C. discussed the results and commented on the manuscript. All authors have read and agreed to the final version of the manuscript.

## References

1 L. Martin, Y.-H. Chu and R. Ramesh, *Materials Science and Engineering: R: Reports*, 2010, **68**, 89–133.

2 D. G. Schlom, L.-Q. Chen, C.-B. Eom, K. M. Rabe, S. K. Streiffer and J.-M. Triscone, *Annu. Rev. Mater. Res.*, 2007, **37**, 589–626.

3 A. Chen, Q. Su, H. Han, E. Enriquez and Q. Jia, *Advanced Materials*, 2019, **31**, 1803241.

4 J. M. Rondinelli and N. A. Spaldin, *Advanced materials*, 2011, **23**, 3363–3381.

5 D. Kan, R. Aso, R. Sato, M. Haruta, H. Kurata and Y. Shimakawa, *Nature materials*, 2016, **15**, 432–437.

6 B. P. Uberuaga, P. P. Dholabhai, G. Pilania and A. Chen, *APL Materials*, 2019, **7**, 100904.

7 H. M. Christen, J. H. Nam, H. S. Kim, A. J. Hatt and N. A. Spaldin, *Physical Review B*, 2011, **83**, 144107.

8 K. T. Kang, B. Zhang, Y. Sharma, B. Paudel, H. Wang, P. Dowden and A. Chen, *Appl. Phys. Lett.*, 2020, **117**, 151601.

9 B. Paudel, I. Vasiliev, M. Hammouri, D. Karpov, A. Chen, V. Lauter and E. Fohtung, *RSC advances*, 2019, **9**, 13033–13041.

10 D. Proffit, H. Jang, S. Lee, C. Nelson, X. Pan, M. Rzchowski and C. Eom, *Applied Physics Letters*, 2008, **93**, 111912.

11 Z. Chen, A. Damodaran, R. Xu, S. Lee and L. Martin, *Applied Physics Letters*, 2014, **104**, 182908.

12 A. Vailionis, H. Boschker, Z. Liao, J. Smit, G. Rijnders, M. Huijben and G. Koster, *Applied physics letters*, 2014, **105**, 131906.

13 W. Li, B. Zhu, Q. He, A. Y. Borisevich, C. Yun, R. Wu, P. Lu, Z. Qi, Q. Wang, A. Chen, H. Wang, S. A. Cavill, K. H. L. Zhang and J. L. MacManus-Driscoll, *Adv. Sci.*, 2020, **7**, 1901606.

14 J. He, A. Borisevich, S. V. Kalinin, S. J. Pennycook and S. T. Pantelides, *Physical review letters*, 2010, **105**, 227203.

15 S. H. Chang, Y. J. Chang, S. Jang, D. Jeong, C. Jung, Y.-J. Kim, J.-S. Chung and T. Noh, *Physical Review B*, 2011, **84**, 104101.

16 M. Gu, Q. Xie, X. Shen, R. Xie, J. Wang, G. Tang, D. Wu, G. Zhang and X. Wu, *Physical Review Letters*, 2012, **109**, 157003.

17 E.-J. Guo, R. Desautels, D. Keavney, M. A. Roldan, B. J. Kirby, D. Lee, Z. Liao, T. Charlton, A. Herklotz and T. Z. Ward, *Science advances*, 2019, **5**, eaav5050.

18 J. E. Boschker, Å. F. Monsen, M. Nord, R. Mathieu, J. K. Grepstad, R. Holmestad, E. Wahlström and T. Tybell, *Philosophical Magazine*, 2013, **93**, 1549–1562.

19 Y.-H. Chu, L. W. Martin, M. B. Holcomb and R. Ramesh, *Materials Today*, 2007, **10**, 16–23.

20 H. W. Jang, D. Ortiz, S. Baek, C. M. Folkman, R. R. Das, P. Shafer, Y. Chen, C. T. Nelson, X. Pan and R. Ramesh, *Advanced materials*, 2009, **21**, 817–823.

21 F. Johann, A. Morelli, D. Biggemann, M. Arredondo and I. Vrejoiu, *Physical Review B*, 2011, **84**, 094105.

22 M. Zhuo, Y. Zhu, X. Ma and H. Lu, *Applied physics letters*, 2006, **88**, 071905.

23 M. Mathews, F. M. Postma, J. C. Lodder, R. Jansen, G. Rijnders and D. H. Blank, *Applied Physics Letters*, 2005, **87**, 242507.

24 Z.-H. Wang, G. Cristiani and H.-U. Habermeier, *Applied physics letters*, 2003, **82**, 3731–3733.

25 R. Mahesh, R. Mahendiran, A. Raychaudhuri and C. Rao, .

26 O. Lebedev, G. Van Tendeloo, S. Amelinckx, F. Razavi and H.-U. Habermeier, *Philosophical Magazine A*, 2001, **81**, 797–824.

27 J. Rodriguez-Carvajal, M. Hennion, F. Moussa, A. Moudden, L. Pinsard and A. Revcolevschi, *Physical Review B*, 1998, **57**, R3189.

28 D. E. Cox, T. Iglesias, E. Moshopoulou, K. Hirota, K. Takahashi and Y. Endoh, *Phys. Rev. B*, 2001, **64**, 024431.

29 A. Vailionis, H. Boschker, W. Siemons, E. P. Houwman, D. H. A. Blank, G. Rijnders and G. Koster, *Phys. Rev. B*, 2011, **83**, 064101.

30 A. Urushibara, Y. Moritomo, T. Arima, A. Asamitsu, G. Kido and Y. Tokura, *Phys. Rev. B*, 1995, **51**, 14103–14109.

31 Q. Gan, R. A. Rao and C. B. Eom, *Appl. Phys. Lett.*, 1997, **70**, 1962–1964.

32 U. Gebhardt, N. V. Kasper, A. Vigliante, P. Wochner, H. Dosch, F. S. Razavi and H.-U. Habermeier, *Phys. Rev. Lett.*, 2007, **98**, 096101.

33 B. Paudel, B. Zhang, Y. Sharma, K. T. Kang, H. Nakotte, H. Wang and A. Chen, *Appl. Phys. Lett.*, 2020, **117**, 081903.

34 J. E. Boschker, C. Folkman, C. W. Bark, Å. F. Monsen, E. Folven, J. K. Grepstad, E. Wahlström, C. B. Eom and T. Tybell, *Phys. Rev. B*, 2011, **84**, 205418.

35 D. Fuchs, L. Dieterle, E. Arac, R. Eder, P. Adelmann, V. Eyert, T. Kopp, R. Schneider, D. Gerthsen and H. v. Löhneysen, *Phys. Rev. B*, 2009, **79**, 024424.

36 H. Röder, J. Zang and A. R. Bishop, *Phys. Rev. Lett.*, 1996, **76**, 1356–1359.

37 R. Mbatang, D. Xue, E. Enriquez, R. Yuan, H. Han, P. Dowden, Q. Wang, E. Fohtung, D. Xue, T. Lookman, S. J. Pennycook and A. Chen, *Nanoscale*, 2019, **11**, 7364–7370.

38 C. Zhong, X. Lu, Y. Wan, Y. Min, Z. Zhao, P. Zhou, Z. Dong and J. Liu, *Journal of Magnetism and Magnetic Materials*, 2018, **466**, 406–410.

39 M. A. Zurbuchen, W. Tian, X. Q. Pan, D. Fong, S. K. Streiffer, M. E. Hawley, J. Lettieri, Y. Jia, G. Asayama, S. J. Fulk, D. J. Comstock, S. Knapp, A. H. Carim and D. G. Schlom, *J. Mater. Res.*, 2007, **22**, 1439–1471.

40 K. P. McKenna, F. Hofer, D. Gilks, V. K. Lazarov, C. Chen, Z. Wang and Y. Ikuhara, *Nat Commun*, 2014, **5**, 5740.

41 C. Ma, M. Liu, C. Chen, Y. Lin, Y. Li, J. S. Horwitz, J. Jiang, E. I. Meletis and Q. Zhang, *Sci Rep*, 2013, **3**, 3092.

42 J. C. Jiang, Y. Lin, C. L. Chen, C. W. Chu and E. I. Meletis, *Journal of Applied Physics*, 2002, **91**, 3188–3192.

43 A. Chen, Z. Bi, C. Tsai, J. Lee, Q. Su, X. Zhang, Q. Jia, J. L. MacManus-Driscoll and H. Wang, *Advanced Functional Materials*, 2011, **21**, 2423–2429.